

# Analyzing intermittent stochastic gravitational wave background I: Effect of detector response

Xiaolin Liu<sup>1,\*</sup> and Sachiko Kuroyanagi<sup>†,2,‡</sup>

<sup>1</sup>*Instituto de Física Teórica UAM-CSIC, Universidad Autónoma de Madrid, Cantoblanco 28049 Madrid, Spain*

<sup>2</sup>*Department of Physics, Nagoya University, Chikusa, Nagoya 464-8602, Japan*

With the growing number of gravitational-wave detections, particularly from binary black hole mergers, there is increasing anticipation that an astrophysical background, formed by an ensemble of faint, high-redshift events, will be observed in the near future by the ground-based detector network. This background is anticipated to exhibit non-Gaussian statistical properties. To develop a robust method for detecting such a non-Gaussian gravitational-wave background, we revisit optimal detection strategies based on the Gaussian-mixture likelihood model. In this work, we demonstrate that properly accounting for the detector antenna pattern is essential. Current approaches typically rely on the overlap reduction function averaged over the sky. Through simulations, we show that using such an averaged response introduces significant biases in parameter estimation. In addition, we propose a computationally feasible method that incorporates second-order corrections as an approximation of the full integral over the source distribution. Our results indicate that this approach effectively eliminates these biases. We also show that our method remains robust even when considering anisotropic backgrounds.

## I. INTRODUCTION

Remarkable progress has been made in gravitational wave (GW) detection in recent years. The ground-based detector network operated by the LIGO-Virgo-KAGRA (LVK) collaboration [1–3] has successfully detected numerous GW events [4–6], including binary black holes (BBHs), binary neutron stars, and black hole-neutron star mergers. With planned upgrades to existing detectors and the development of next-generation facilities such as the Einstein Telescope (ET) [7] and Cosmic Explorer (CE) [8], along with space-based observatories like LISA [9], TianQin [10], Taiji [11], B-DECIGO and DECIGO [12], we will be able to probe a wider frequency spectrum with significantly enhanced sensitivity. This will allow the detection of more GW signals, including increasingly faint sources. Among these targets, the gravitational wave background (GWB) remains a particularly important focus [13, 14].

Stochastic GWB refers to a random and persistent background of GWs. There are many possible sources of GWB signals, including astrophysical sources such as compact binary coalescing (CBC) systems, supernova explosions, and cosmological processes such as inflation and phase transitions. Typically, the dimensionless energy density  $\Omega_{\text{gw}}$  is used to describe the strength of the GWB:

$$\Omega_{\text{gw}}(f) = \frac{1}{\rho_c} \frac{d\rho_{\text{gw}}}{d \ln f}, \quad (1)$$

where  $\rho_{\text{gw}}$  is the energy density of the GWB and  $\rho_c = 3H_0^2/(8\pi G)$  is the critical energy density of the Universe

today with  $H_0$  being the Hubble parameter at present time. The observed individual BBH systems in the LVK O4a run provide insights into the merger rate and redshift distribution of stellar-mass binaries, which can have implications for the amplitude of the astrophysical background. This suggests  $\Omega_{\text{gw}}(25\text{Hz}) = 0.9_{-0.5}^{+1.1} \times 10^{-9}$ , a value that may be detectable with the sensitivity of the O5 run [15]. Measuring such an astrophysical background is essential for understanding the black hole formation history [16, 17].

Detecting the GWB has long been a challenge due to its weak intensity. Achieving a higher signal-to-noise ratio (SNR) requires long-term observational data and cross-correlation between multiple detectors to suppress the influence of noise [18]. For the astrophysical background from stellar-mass BBH systems, the average duration of GW signals is shorter than the average interval between two consecutive BBH mergers in the frequency band of ground-based detectors, leading to an intermittent distribution of signals in the data [19–21]. The duty cycle,  $\xi$ , quantifies this intermittency by representing the fraction of the total data occupied by GW signals [22]. A lower  $\xi$  implies a higher degree of non-Gaussianity in the strain distribution. This measure is valuable for inferring the origins and populations of BBHs [23].

Drasco and Flanagan [24] were the first to develop a systematic theoretical framework for detecting non-Gaussian GWB. This framework was later generalized to include the conventional cross-correlation model applied to spatially separated interferometers with colored, non-Gaussian noise such as glitches [25]. It has been shown that these non-Gaussian statistics can significantly enhance detection efficiency compared to standard cross-correlation search methods, particularly at low  $\xi$  [26].

In addition, there have been proposals to utilize higher-order statistics. Theoretically, if the properties of noise and the GW signal are well understood and modeled properly, higher-order statistical measures can enhance

<sup>†</sup>corresponding author

<sup>\*</sup>Xiaolin Liu: shallyn.liu@foxmail.com

<sup>‡</sup>Sachiko Kuroyanagi: sachiko.kuroyanagi@csic.es

detection efficiency [27, 28]. Seto [29, 30] introduced detection methods fourth-order statistical quantities and cumulants using four-detector. The work has focused on non-Gaussian statistical properties arising from the intermittency of the GW signal, with the resulting kurtosis parameter being characterized by the duty cycle  $\xi$ . In contrast, Martellini and Regimbau [31, 32] addressed non-Gaussianity in signal distributions and proposed semiparametric maximum likelihood estimators to estimate higher-order moments via a fourth-order Edgeworth expansion, and provided detailed comparisons between second-order and fourth-order statistics. Application of a heavy-tailed Generalized Hyperbolic function has been discussed in [33].

Other approaches also have been extensively developed. One prominent method involves using subthreshold BBHs in matched-filtering searches combined with Bayesian statistics to infer the duty cycle [34–37]. In addition, spectrogram correlated stacking has been proposed to leverage higher-order statistics in the time-frequency domain [38–40]. Finally, there has also been new effort to apply deep learning methods to the search for non-Gaussian backgrounds [41, 42].

The non-Gaussian level in the astrophysical background is determined by three factors: **intermittency, sample distribution, and waveform**. Intermittency is particularly significant for the BBH background, which is expected to exhibit an extremely low duty cycle,  $\xi \sim \mathcal{O}(10^{-3})$ . This aspect is typically modeled using a Gaussian mixture framework [24], where the likelihood comprises two Gaussian components representing segments with and without signals. The segments containing signals are often assumed to have strain amplitudes that follow a Gaussian distribution, based on the central limit theorem. However, this assumption may not hold due to the limited number of samples or when the samples are drawn from a heavy-tailed power-law distribution, which can occur when the sample is taken assuming the typical BBH population. Indeed, recent studies have shown that the statistical properties of the GWB strongly depend on the BBH population, including their mass and redshift distributions [39]. Furthermore, the GW waveform produced by BBH systems exhibits inherent non-Gaussian characteristics. Recent work in the context of pulsar timing [43] has indicated that the higher-order statistical frequency spectrum of the astrophysical GWB follows a power-law behavior. These properties are closely related to the distinctive dynamical evolution of BBH systems.

In light of these considerations, the analysis method can be enhanced by incorporating additional non-Gaussian aspects, underscoring the importance of accurately modeling such distributional properties. In this paper, we emphasize that, beyond the three factors discussed above, properly accounting for the detector response is crucial for intermittent searches. Because GW detectors have specific non-isotropic antenna patterns, even if the intrinsic GW signal follows a Gaussian distribution, the projected amplitude becomes distorted. We

quantify this effect and propose a computationally efficient method to incorporate it. Furthermore, we demonstrate that neglecting this contribution introduces systematic biases in the estimation of key parameters, such as the duty cycle and GW amplitude.

This work is the first in a series of papers. In this paper, we focus on the effect of the antenna pattern function. To present this in a simple framework, we assume intermittent stochastic burst signals, meaning we do not model individual waveforms that compose the stochastic background. We simulate detection using a likelihood based on the Gaussian mixture model [24], modified to incorporate the modulation introduced by the detector response. In a subsequent paper, we will consider more realistic signals, specifically sub-threshold BBH events, and present a detection method based on a fully non-Gaussian likelihood that accounts for all relevant non-Gaussian factors arising not only from intermittency but also from source sample distribution and waveform characteristics.

The paper is organized as follows: In Sec. II, we review the current detection methods for an intermittent background and introduce basic setups for the simulation. In Sec. III, we analyze the effect of detector response on intermittent searches and propose a computationally efficient method to incorporate this effect. We also examine the impact of anisotropic source distributions. In Sec. IV, we present simulation results for signal detection and parameter estimation, comparing different likelihood models and demonstrating how the modified likelihood mitigates parameter bias. We further investigate whether incorrectly assuming an isotropic background when the true distribution is anisotropic introduces additional bias. Finally, Sec. V provides a summary of our findings.

## II. INTERMITTENT SEARCH AND CROSS-CORRELATION

### A. The Gaussian mixture model

Intermittency is typically characterized by a quantity called the duty cycle  $\xi$ , which ranges from 0 to 1 and represents the fraction of data segments containing a GW signal [24]. More specifically, if the observational data over a given period is divided into  $K$  segments, the duty cycle can be approximated as,  $\xi \approx N_{\text{gw}}/K$  where  $N_{\text{gw}}$  is the number of segments that contain GW signals and  $K$  is the total number of segments. Typically, time-series data is divided into short segments optimized for the target signal. For the BBH background, a segment length of about 4 seconds is commonly chosen to ensure that a single signal (with a duration of  $\sim 1$ s) is contained within one segment, while still being long enough to provide a stable noise estimate.

It is important to note that the definition of such data-driven duty cycle involves some ambiguity. Recently, a potential bias in parameter estimation caused

by segment size was highlighted in [44]. Furthermore, it depends on the detector sensitivity, as events with extremely low SNR ( $\ll 1$ ), which are typically numerous, do not contribute to the analysis [23]. Naively, one might set the threshold for inclusion in the analysis based on the matched-filtering SNR of each event to be larger than 1; however, it remains unclear whether this is an appropriate or optimal choice for the threshold.

In contrast, the duty cycle can also be calculated theoretically by counting the number of events that constitute the GWB and accounting for the duration of each event [22, 23, 45]. Establishing a robust connection between the theoretical and data-driven duty cycles remains a challenge due to these ambiguities. This is essential for extracting astrophysical information from the data, but is beyond the scope of this paper. In this work, we generate mock data by injecting Gaussian bursts, ensuring that each signal-containing segment is occupied by a burst-like signal whose amplitude is drawn from a Gaussian distribution. Therefore, we do not expect this ambiguity to arise.

Drasco and Flanagan [24] were the first to propose using a Gaussian mixture model to develop detection statistics optimized for non-Gaussian backgrounds. Let  $\mathcal{L}_s(\mathbf{s}|\mathcal{H}_0)$  and  $\mathcal{L}_n(\mathbf{s}|\mathcal{H}_1)$  denote the likelihood functions for the data  $\mathbf{s}$  under the hypotheses  $\mathcal{H}_0$  (no GW signal) and  $\mathcal{H}_1$  (GW signal present), respectively. Using the duty cycle  $\xi$ , the total likelihood can be expressed as a mixture of these two hypotheses:

$$\mathcal{L}_{\text{tot}}(\mathbf{s}) = \prod_i \xi \mathcal{L}_s(\mathbf{s}_i|\mathcal{H}_1) + (1 - \xi) \mathcal{L}_n(\mathbf{s}_i|\mathcal{H}_0), \quad (2)$$

where  $i$  denotes the index of each data segment. This formulation arises from assuming that the distribution of the GW strain amplitude  $h$  takes the form of

$$p_{h,\text{tot}}(h) = \xi p_h(h) + (1 - \xi) \delta(h), \quad (3)$$

where  $p_h(h)$  is the distribution of the strain amplitude for a GW event (e.g., a BBH event), and  $\delta(h)$  is the delta function representing segments with no signal. In this framework, the amplitude of the GWB is characterized by the variance of this distribution.

The distribution  $p_h(h)$  is often assumed to be Gaussian, primarily because, in an ideal scenario with a large volume of observational data, the dataset would contain multiple independent GW signals. Under these conditions,  $p_h(h)$  would closely approximate a Gaussian distribution due to the central limit theorem. In the context of intermittent searches for the BBH background, however, this assumption may not hold. Nevertheless, in this paper, we focus on the effect of the antenna pattern function and therefore assume a Gaussian distribution for the original signal amplitudes. This choice simplifies the analysis and allows us to clearly isolate and study the impact of the antenna pattern.

## B. Cross-correlating detectors in different locations

In this work, we remove the commonly assumed setup of co-aligned and co-located detectors. By doing so, we are required to consider the response of cross-correlated detectors, which is often described by the overlap reduction function [18]. One of the key points of this paper is that accounting for the antenna pattern function introduces non-trivial effects on the signal distribution, as the response is not spherically symmetric and alters the distribution of the projected GW strain amplitude. We describe the details of our setup below.

For ground-based detectors, where the light travel time along the arms is short compared to the GW period, the antenna pattern function in the small-antenna limit can be approximated as

$$F_A(\hat{\Omega}) = \frac{1}{2} e_A^{ab}(\hat{\Omega}) \left( \hat{l}_1^a \hat{l}_1^b - \hat{l}_2^a \hat{l}_2^b \right), \quad (4)$$

where  $\hat{\Omega}$  is the direction in which the GWs propagate,  $\hat{l}_{1,2}$  are the unit vectors describing the two arms of the detector, and  $e_A^{ab}$  with  $A = +, \times$  are transverse-traceless polarization tensors,

$$e_+^{ab}(\hat{\Omega}) = \hat{p}^a \hat{p}^b - \hat{q}^a \hat{q}^b, \quad (5)$$

$$e_\times^{ab}(\hat{\Omega}) = \hat{p}^a \hat{q}^b + \hat{q}^b \hat{p}^a. \quad (6)$$

Here,  $\hat{p}$  and  $\hat{q}$  are vectors perpendicular to each other and to  $\hat{\Omega}$ . Considering the earth's rotation, we have [46]

$$F_+(\hat{\Omega}) = \sin \zeta (\cos 2\psi G_+(\hat{\Omega}) + \sin 2\psi G_\times(\hat{\Omega})), \quad (7)$$

$$F_\times(\hat{\Omega}) = \sin \zeta (\cos 2\psi G_\times(\hat{\Omega}) - \sin 2\psi G_+(\hat{\Omega})), \quad (8)$$

and  $G_{+,\times}$  are given by

$$\begin{aligned} G_+(\hat{\Omega}) &= \frac{1}{4} \cos(\alpha - \varphi - \omega_\oplus t) \sin 2\beta \sin 2\delta \sin 2\lambda \\ &+ \frac{1}{16} (3 - \cos 2\delta)(3 - \cos 2\lambda) \cos 2(\alpha - \varphi - \omega_\oplus t) \sin 2\beta \\ &- \frac{1}{2} \cos 2\beta \cos \lambda \sin 2\delta \sin(\alpha - \varphi - \omega_\oplus t) \\ &- \frac{1}{4} \cos 2\beta (3 - \cos 2\delta) \sin \lambda \sin 2(\alpha - \varphi - \omega_\oplus t) \\ &+ \frac{3}{4} \cos^2 \delta \cos^2 \lambda \sin 2\beta, \end{aligned} \quad (9)$$

$$\begin{aligned} G_\times(\hat{\Omega}) &= \cos 2\beta \cos \delta \cos \lambda \cos(\alpha - \varphi - \omega_\oplus t) + \\ &+ \cos 2\beta \cos 2(\alpha - \varphi - \omega_\oplus t) \sin \delta \sin \lambda \\ &+ \frac{1}{2} \cos \delta \sin 2\beta \sin 2\lambda \sin(\alpha - \varphi - \omega_\oplus t) \\ &+ \frac{1}{4} (3 - \cos 2\lambda) \sin 2\beta \sin \delta \sin 2(\alpha - \varphi - \omega_\oplus t), \end{aligned} \quad (10)$$

where  $(\zeta, \lambda, \varphi, \beta)$  are parameters characterizing the detector:  $\zeta$  is the angle between the detector's arms,  $\lambda$  and  $\varphi$  are the detector's latitude and longitude, respectively, and  $\beta$  is the angle between the arm bisector and the East

direction. The parameters  $(\alpha, \delta)$  represent the right ascension and declination of the source direction  $\hat{\Omega}$ , and  $\omega_{\oplus}$  is the Earth's rotational angular velocity; for simplicity, this term is omitted.

As convention, we consider the decomposition of the tensor metric perturbations  $h_{ab}$  into the Fourier modes using the two independent polarization states

$$h_{ab}(t, \mathbf{x}) = \sum_A \int_{-\infty}^{\infty} df \int_{S^2} d\hat{\Omega} \tilde{H}_A(f, \hat{\Omega}) e^{i2\pi f(t - \hat{\Omega} \cdot \mathbf{x})} e_{ab}^A(\hat{\Omega}), \quad (11)$$

where  $\mathbf{x}$  describes the location of the detector and  $\tilde{H}_A(f, \hat{\Omega})$  is the amplitude of each polarization mode. Now, let us explicitly retain the anisotropy of the background in order to examine the effect of the antenna pattern function. For a stationary, Gaussian, and unpolarized background, the amplitudes satisfy the following statistical properties,

$$\begin{aligned} & \langle \tilde{H}_A^*(f, \hat{\Omega}) \tilde{H}_{A'}(f', \hat{\Omega}') \rangle \\ &= \frac{1}{4} \delta_{A,A'} \delta(f - f') \frac{1}{4\pi} \delta^2(\hat{\Omega}, \hat{\Omega}') \mathcal{P}_H(f, \hat{\Omega}), \end{aligned} \quad (12)$$

where the power spectral density  $\mathcal{P}_H(f, \hat{\Omega})$  characterizes both the spectral and angular distribution of the background and is assumed to factorize as  $\mathcal{P}_H(f, \hat{\Omega}) = P_H(f) \mathcal{P}(\hat{\Omega})$  with  $\int d\hat{\Omega} \mathcal{P}(\hat{\Omega}) = 4\pi$ . The factor 1/4 is included by convention to account for the one-sided definition of the strain power spectrum and summing the two polarization states, while the 1/4 $\pi$  factor reflects the normalization over the unit sphere<sup>1</sup>. Then it is related to the GW energy density parameter as

$$\Omega_{\text{gw}} = \frac{2\pi^2}{3H_0^2} f^3 \frac{1}{4\pi} \int d\hat{\Omega} \mathcal{P}_H(f, \hat{\Omega}). \quad (13)$$

Note that, for an intermittent background, the energy density should be multiplied by the duty cycle  $\xi$ , which represents the fraction of time during which the signal is present, effectively reducing the observed energy density compared to a continuous background.

Using the antenna pattern function, the GW signal measured at the detector  $I$  in the Fourier space is given by

$$\tilde{H}_I(f) = \sum_A \int_{S^2} d\hat{\Omega} \tilde{H}_A(f, \hat{\Omega}) F_{I,A}(\hat{\Omega}) e^{-i2\pi f \hat{\Omega} \cdot \mathbf{x}_I}. \quad (14)$$

In GWB searches with ground-based detectors, the data is divided into short time segments and analyzed in the

discrete Fourier domain. For a segment that contains a GW signal, the observable  $\tilde{s}$  in detector  $I$  in the  $i$ -th data segment can be expressed as:

$$\tilde{s}_{I,i}(f) = \tilde{n}_{I,i}(f) + \tilde{H}_{I,i}(f), \quad (15)$$

where  $\tilde{n}_{I,i}$  represents the detector noise in Fourier space.

When performing cross-correlation between two detectors, the noise terms are suppressed under the assumption that the noise is uncorrelated, and the expectation value of the cross-correlated data can be approximated as

$$\begin{aligned} & \langle \tilde{s}_{I,i}^*(f) \tilde{s}'_{J,i}(f) \rangle \simeq \langle \tilde{H}_{I,i}^*(f) \tilde{H}'_{J,i}(f) \rangle \\ &= \sum_{A,A'} \int_{S^2} d\hat{\Omega} \int_{S^2} d\hat{\Omega}' \langle \tilde{H}_A^*(f, \hat{\Omega}) \tilde{H}_{A'}(f', \hat{\Omega}') \rangle \\ & \quad \times F_{I,A}(\hat{\Omega}) F_{J,A'}(\hat{\Omega}') e^{i2\pi f \hat{\Omega} \cdot (\mathbf{x}_I - \mathbf{x}_J)}. \end{aligned} \quad (16)$$

For an isotropic background,  $\tilde{H}_A(f, \hat{\Omega})$  becomes independent of direction and we can set  $\mathcal{P}(\hat{\Omega}) = 1$ . In this case, by substituting Eq. (12), Eq. (16) simplifies to [18]

$$\langle \tilde{s}_{I,i}^*(f) \tilde{s}'_{J,i}(f) \rangle \simeq \frac{1}{10} \delta(f - f') P_H(f) \bar{\gamma}_{IJ}(f), \quad (17)$$

where the overlap reduction function is defined as

$$\bar{\gamma}_{IJ}(f) := \frac{5}{8\pi} \sum_A \int_{S^2} d\hat{\Omega} F_{I,A}(\hat{\Omega}) F_{J,A}(\hat{\Omega}) e^{i2\pi f \hat{\Omega} \cdot (\mathbf{x}_1 - \mathbf{x}_2)}. \quad (18)$$

In the case of the intermittent astrophysical background, the signal is not isotropic in each segment. Instead, it behaves like a point source, which can be modeled as:  $\mathcal{P}(\hat{\Omega}) = 4\pi \delta^2(\hat{\Omega}, \hat{\Omega}_i)$  with  $\hat{\Omega}_i$  representing the GW direction in  $i$ -th data segment. By explicitly leaving the directional dependence, Eq. (16) leads to

$$\langle \tilde{s}_{I,i}^*(f) \tilde{s}'_{J,i}(f) \rangle \simeq \frac{1}{4} \delta(f - f') P_H(f) \gamma_{IJ}(f, \hat{\Omega}_i), \quad (19)$$

where

$$\gamma_{IJ}(f, \hat{\Omega}_i) := \sum_A F_{I,A}(\hat{\Omega}_i) F_{J,A}(\hat{\Omega}_i) e^{i2\pi f \hat{\Omega}_i \cdot (\mathbf{x}_1 - \mathbf{x}_2)}. \quad (20)$$

We typically assume a uniform distribution of astrophysical sources over the sky, and take the ensemble average over source directions which is denoted as  $\langle \gamma_{IJ}(f, \hat{\Omega}_i) \rangle_{\hat{\Omega}_i}$ . This averaging leads to  $\langle \gamma_{IJ}(f, \hat{\Omega}_i) \rangle_{\hat{\Omega}_i} = 2\bar{\gamma}_{IJ}(f)/5$  and it becomes effectively equivalent to the isotropic case [48].

### C. Likelihood function

Let us assume that the noise is stationary, Gaussian-distributed, and that its real and imaginary components in the Fourier domain, as well as different frequency bins, are statistically independent. Under these assumptions,

<sup>1</sup> Our definition differs from that used in anisotropic background searches (see e.g., [47]) by a factor of 1/4 $\pi$ . This is because, in our case, the the GWB amplitude of interest remains isotropic after summing over contributions from all directions. In contrast, anisotropic searches focus on continuous sources with directional dependence, where the signal is localized or enhanced in a specific direction.

the probability density function of the noise can be expressed as

$$p_{n_I}(\tilde{n}_I(f)) = \mathbf{G}[\sigma_{n_I}^2(f)](\text{Re } \tilde{n}_I(f))\mathbf{G}[\sigma_{n_I}^2(f)](\text{Im } \tilde{n}_I(f)), \quad (21)$$

where  $\mathbf{G}[\sigma^2](x) := e^{-x^2/(2\sigma^2)}/\sqrt{2\pi\sigma^2}$  denotes the standard Gaussian distribution function. Here, we explicitly separate the real and imaginary parts of the noise. The variance  $\sigma_{n_I}^2(f)$  is defined as

$$\sigma_{n_I}^2(f) := \frac{T_{\text{seg}}}{4} P_{n_I}(f), \quad (22)$$

where  $T_{\text{seg}}$  is the duration of the data segment, and  $P_{n_I}(f)$  is the noise power spectral density of detector  $I$ .

So far, we have expressed quantities as continuous functions of frequency. However, in practice, we work with discrete frequency bins defined by  $f_k = k\Delta f$  with  $\Delta f = 1/T_{\text{seg}}$  being the frequency resolution determined by the segment duration  $T_{\text{seg}}$ . The likelihood function is then constructed as a product over the likelihoods of individual frequency bins. For a signal-absent segment, the likelihood function  $\mathcal{L}_n(\mathbf{s}_i|\mathcal{H}_0)$  is given by

$$\mathcal{L}_n(\tilde{s}_i|\sigma_n^2) = \prod_k \prod_I \frac{1}{2\pi\sigma_{n_I}^2(f_k)} \exp \left[ -\frac{1}{2} \frac{\tilde{s}_{I,i}^*(f_k)\tilde{s}_{I,i}(f_k)}{\sigma_{n_I}^2(f_k)} \right]. \quad (23)$$

Assuming that the GW signal  $\tilde{H}_A$  follows a Gaussian distribution, its probability density function is given by:

$$p_{\text{gw}}(\tilde{H}_A(f)) = \mathbf{G}[\sigma_H^2(f)](\text{Re } \tilde{H}_A(f))\mathbf{G}[\sigma_H^2(f)](\text{Im } \tilde{H}_A(f)), \quad (24)$$

where  $\gamma_{IJ}$  is the non-averaged overlap reduction function defined in Eq. (20) and we define

$$|\gamma_I|^2(\hat{\Omega}_i) := \sum_A |F_{I,A}(\hat{\Omega}_i)|^2. \quad (29)$$

In practical detection scenarios, evaluating the integral over  $d\hat{\Omega}$  is computationally challenging. One approach commonly adopted in previous studies to simplify the analysis is to assume a uniform prior  $p_\Omega$  over the sky and replace  $\gamma_{IJ}(f, \hat{\Omega}_i)$  and  $|\gamma_I|^2(\hat{\Omega}_i)$  with their directional averages  $\langle \gamma_{IJ}(f, \hat{\Omega}_i) \rangle_{\hat{\Omega}_i} = 2\bar{\gamma}_{IJ}(f)/5$  and  $\langle |\gamma_I|^2(\hat{\Omega}_i) \rangle_{\hat{\Omega}_i} = 2/5$ , respectively. This approximation removes the  $\hat{\Omega}_i$ -dependence from the covariance matrix and simplify the calculation. We denote this direction-averaged covari-

where

$$\sigma_H^2(f) := \frac{T_{\text{seg}}}{2} P_H(f), \quad (25)$$

representing the variance of the GW signal in the Fourier domain. This variance relates to the intensity of the GWB that we aim to detect, with  $\Omega_{\text{gw}}(f) \propto \xi \sigma_H^2(f)$ .

Accordingly, we can construct the likelihood function of the signal segment  $\mathcal{L}_s(\mathbf{s}_i|\mathcal{H}_1)$  as

$$\begin{aligned} \mathcal{L}_s(\tilde{s}_i|\sigma_n^2, \sigma_H^2) &= \prod_k \int \prod_I p_{n_I}(\tilde{s}_{I,i} - F_{I,A}(\hat{\Omega}_i) e^{-i2\pi f \hat{\Omega}_i \cdot \mathbf{x}_I} \tilde{H}_A(f_k)) \\ &\quad \times p_{\text{gw}}(\tilde{H}_A(f_k)) p_\Omega(\hat{\Omega}_i) d\tilde{H}_A(f_k) d\hat{\Omega}_i. \end{aligned} \quad (26)$$

Here,  $p_\Omega(\hat{\Omega}_i)$  is the probability density function of GW direction  $\hat{\Omega}_i$ . Substituting the Gaussian distributions and performing the integral, one would obtain [19, 49]:

$$\begin{aligned} \mathcal{L}_s(\tilde{s}_i|\sigma_n^2, \sigma_H^2) &= \prod_k \int \frac{1}{\det[2\pi\mathbb{C}(f_k, \hat{\Omega}_i)]} \\ &\quad \times \exp \left[ -\frac{1}{2} \sum_{IJ} \tilde{s}_{I,i}^*(\mathbb{C}^{-1}(f_k, \hat{\Omega}_i))_{IJ} \tilde{s}_{J,i} \right] p_\Omega(\hat{\Omega}_i) d\hat{\Omega}_i, \end{aligned} \quad (27)$$

where  $\mathbb{C}$  is the covariance matrix, given by:

$$\mathbb{C}(f_k, \hat{\Omega}_i) := \begin{bmatrix} \sigma_{n_1}^2(f_k) + |\gamma_1|^2(\hat{\Omega}_i) \sigma_H^2(f_k) & \gamma_{12}(f_k, \hat{\Omega}_i) \sigma_H^2(f_k) & \dots \\ \gamma_{12}^*(f_k, \hat{\Omega}_i) \sigma_H^2(f_k) & \sigma_{n_2}^2(f_k) + |\gamma_2|^2(\hat{\Omega}_i) \sigma_H^2(f_k) & \dots \\ \dots & \dots & \dots \end{bmatrix}, \quad (28)$$

ance matrix as  $\langle \mathbb{C} \rangle_{\hat{\Omega}_i}$  for later use,

$$\langle \mathbb{C} \rangle_{\hat{\Omega}_i}(f_k) := \begin{bmatrix} \sigma_{n_1}^2(f_k) + \frac{2}{5}\sigma_H^2(f_k) & \frac{2}{5}\bar{\gamma}_{12}(f_k)\sigma_H^2(f_k) & \dots \\ \frac{2}{5}\bar{\gamma}_{12}(f_k)\sigma_H^2(f_k) & \sigma_{n_2}^2(f_k) + \frac{2}{5}\sigma_H^2(f_k) & \dots \\ \dots & \dots & \dots \end{bmatrix}. \quad (30)$$

However, as we will discuss in the following section, this simplification introduces certain limitations.

### III. EFFECT OF DETECTOR RESPONSE

The intermittent search is performed to maximize the likelihood function, given in Eq. (2). The noise-related and signal-related likelihood terms,  $\mathcal{L}_n(\mathbf{s}_i|\mathcal{H}_0)$

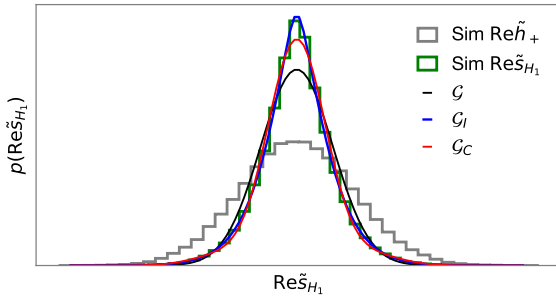


FIG. 1: Schematic representation of the deformation in the GWB distribution after projection onto the detector  $H_1$ . The grey and green histograms show the distribution of  $\text{Re } \tilde{h}_+$  (Gaussian) and the received signal by the detector  $\text{Re } \tilde{s}_{H_1}$ , respectively. Solid curves indicate three different theoretical predictions: the blue curve ( $\mathcal{G}_I$ ) shows the fully integrated model calculated as in Eq. (28), the red curve ( $\mathcal{G}_C$ ) depicts the Gaussian distribution corrected by the second-order covariance matrix  $\Gamma_{ab}$  as in Eq. (31), and the black curve ( $\mathcal{G}$ ) represents the leading-order Gaussian approximation.

and  $\mathcal{L}_s(\mathbf{s}_i|\mathcal{H}_1)$ , are now given by Eq. (23) and Eq. (27), respectively. In this section, we discuss how using the direction-averaged covariance matrix  $\langle \mathbb{C} \rangle_{\hat{\Omega}_i}$ , given in Eq. (30), instead of performing integration over  $\hat{\Omega}_i$  in Eq. (27), introduces biases in parameter estimation.

### A. Accounting for antenna pattern as second-order corrections

The cause of the discrepancy between using  $\langle \mathbb{C} \rangle_{\hat{\Omega}_i}$  and  $\mathbb{C}_{\hat{\Omega}_i}$  may be interpreted as follows. When employing the direction-averaged covariance matrix  $\langle \mathbb{C} \rangle_{\hat{\Omega}_i}$ , the likelihood function is effectively equivalent to assuming that the observed GW signal at detector  $I$ ,  $\tilde{H}_{A,I}(f_k) = \sqrt{\frac{2}{5}} F_{I,A}(\hat{\Omega}) e^{-i 2\pi f_k \hat{\Omega}_i \cdot \mathbf{x}_I} \tilde{H}_A(f_k)$  follows a Gaussian distribution. However, in reality, due to the non-trivial structure of the antenna pattern function, the projected signal  $\tilde{H}_{A,I}(f_k)$  exhibits deviations from the Gaussian assumption, even if the original signal itself is Gaussian. By performing the integration in Eq. (27), we can properly account for the deformation of the distribution introduced by the antenna pattern. In contrast, when using the direction-averaged covariance matrix  $\langle \mathbb{C} \rangle_{\hat{\Omega}_i}$ , as in Eq. (30), the assumed likelihood shape deviates from the true distribution and eventually introduce bias in the parameter estimation.

To account for the effect of the antenna patterns, the integration of Eq. (27) must be evaluated numerically. However, this process is computationally expensive. Instead, we propose the Taylor expanded form:

$$\mathcal{L}_s(\tilde{s}_i|\sigma_n^2, \sigma_H^2) = \langle \mathcal{L}_s(\tilde{s}_i|\mathbb{C}(\hat{\Omega}_i)) \rangle_{\hat{\Omega}_i}$$

$$\begin{aligned} &\simeq \mathcal{L}_s(\tilde{s}_i|\langle \mathbb{C} \rangle_{\hat{\Omega}_i}) + \frac{1}{2} \partial_a \partial_b \mathcal{L}_s(\tilde{s}_i|\langle \mathbb{C} \rangle_{\hat{\Omega}_i}) \Gamma_{ab} \\ &\quad + \mathcal{O}\left(\langle y - \langle y \rangle_{\hat{\Omega}_i} \rangle_{\hat{\Omega}_i}^3\right), \end{aligned} \quad (31)$$

where

$$\begin{aligned} \mathcal{L}_s(\tilde{s}_i|\mathbb{C}(\hat{\Omega}_i)) &:= \prod_k \frac{1}{\det[2\pi \mathbb{C}(f_k, \hat{\Omega}_i)]} \\ &\times \exp\left[-\frac{1}{2} \sum_{IJ} \tilde{s}_{I,i}^*(f_k) (\mathbb{C}^{-1}(f_k, \hat{\Omega}_i))_{IJ} \tilde{s}_{J,i}(f_k)\right]. \end{aligned} \quad (32)$$

The partial derivatives of  $\mathcal{L}_s$  are taken with respect to the vector  $\vec{y} = (|\gamma_1|^2, |\gamma_2|^2, \text{Re } \gamma_{12}, \text{Im } \gamma_{12}, \dots)$ , and the covariance matrix  $\Gamma_{ab} := \langle (y^a - \langle y^a \rangle_{\hat{\Omega}_i})(y^b - \langle y^b \rangle_{\hat{\Omega}_i}) \rangle_{\hat{\Omega}_i}$  characterizes the second-order statistical properties of  $\vec{y}$ . The first term in the expansion corresponds to the Gaussian component, namely the likelihood function with the direction-averaged covariance matrix, which represents the leading-order approximation of the full integral over the angular distribution.

Eq. (31) is equivalent to the Edgeworth expansion [50]. This higher-order correction suggests that the likelihood function is no longer Gaussian. The correction term  $\partial_a \partial_b \mathcal{L}_s(\tilde{s}_i|\mathbb{C})$  takes the form

$$\begin{aligned} \frac{1}{2} \partial_a \partial_b \mathcal{L}_s(\tilde{s}_i|\mathbb{C}) &= -\frac{1}{2} \left( \Sigma^{ab} + \tilde{s}_{I,i} \tilde{s}_{J,i}^* \Sigma_{IJ}^{ab} \right. \\ &\quad \left. + \tilde{s}_{I,i} \tilde{s}_{J,i}^* \tilde{s}_{K,i} \tilde{s}_{L,i}^* \Sigma_{IJKL}^{ab} \right) \mathcal{L}_s(\tilde{s}_i|\langle \mathbb{C} \rangle_{\hat{\Omega}_i}), \end{aligned} \quad (33)$$

where

$$\Sigma^{ab} := \mathbb{C}_{\nu\mu}^{-1} \partial_a \partial_b \mathbb{C}_{\mu\nu} - 2 \mathbb{C}_{\tau(\mu}^{-1} \mathbb{C}_{\nu\rho)}^{-1} \partial_a \mathbb{C}_{\mu\nu} \partial_b \mathbb{C}_{\rho\tau}, \quad (34)$$

$$\begin{aligned} \Sigma_{IJ}^{ab} &:= 2 \mathbb{C}_{I\mu}^{-1} \mathbb{C}_{(\nu\rho)}^{-1} \mathbb{C}_{\tau)J}^{-1} \partial_{(a} \mathbb{C}_{\mu\nu} \partial_{b)} \mathbb{C}_{\rho\tau} \\ &\quad - \mathbb{C}_{I\mu}^{-1} \mathbb{C}_{\nu J}^{-1} \partial_a \partial_b \mathbb{C}_{\mu\nu}, \end{aligned} \quad (35)$$

$$\Sigma_{IJKL}^{ab} := -\frac{1}{4} \mathbb{C}_{I\mu}^{-1} \mathbb{C}_{\nu J}^{-1} \mathbb{C}_{K\rho}^{-1} \mathbb{C}_{\tau L}^{-1} \partial_a \mathbb{C}_{\mu\nu} \partial_b \mathbb{C}_{\rho\tau}. \quad (36)$$

The parentheses in the subscript denote the symmetry operation applied to the indices. The underlined symbol within the parentheses signifies that no symmetry operation is applied to it.

This correction causes the detector signal distribution to become steeper. Specifically, this is manifested in the fourth-order cumulant of the  $\text{Re } \tilde{s}_{I,i}$  distribution, i.e., the Kurtosis, becoming positive,

$$\begin{aligned} \text{Var}[\text{Re } \tilde{s}_{I,i}]|_{\sigma_{n_{I,i}}^2=0} &:= \int (\text{Re } \tilde{s}_{I,i})^2 p(\tilde{s}_i|\sigma_{n_{I,i}}^2=0, \sigma_H^2) d\tilde{s}_{I,i} \\ &= \langle \mathbb{C}_{II} \rangle_{\hat{\Omega}_i}^2|_{\sigma_{n_{I,i}}^2=0} = \sigma_H^2 \langle |\gamma_I|^2 \rangle_{\hat{\Omega}_i}, \end{aligned} \quad (37)$$

$$\text{Kurt}[\text{Re } \tilde{s}_{I,i}] :=$$

$$\begin{aligned} &\int (\text{Re } \tilde{s}_{I,i})^4 p(\tilde{s}_i|\sigma_{n_{I,i}}^2=0, \sigma_H^2) d\tilde{s}_{I,i} - 3 \text{Var}[\text{Re } \tilde{s}_{I,i}]|_{\sigma_{n_{I,i}}^2=0} \\ &= 3 \sigma_H^4 \left( \langle |\gamma_I|^4 \rangle_{\hat{\Omega}_i} - \langle |\gamma_I|^2 \rangle_{\hat{\Omega}_i}^2 \right) \equiv 3 \sigma_H^4 \Gamma_{|\gamma_I|^2|\gamma_I|^2} > 0, \end{aligned} \quad (38)$$

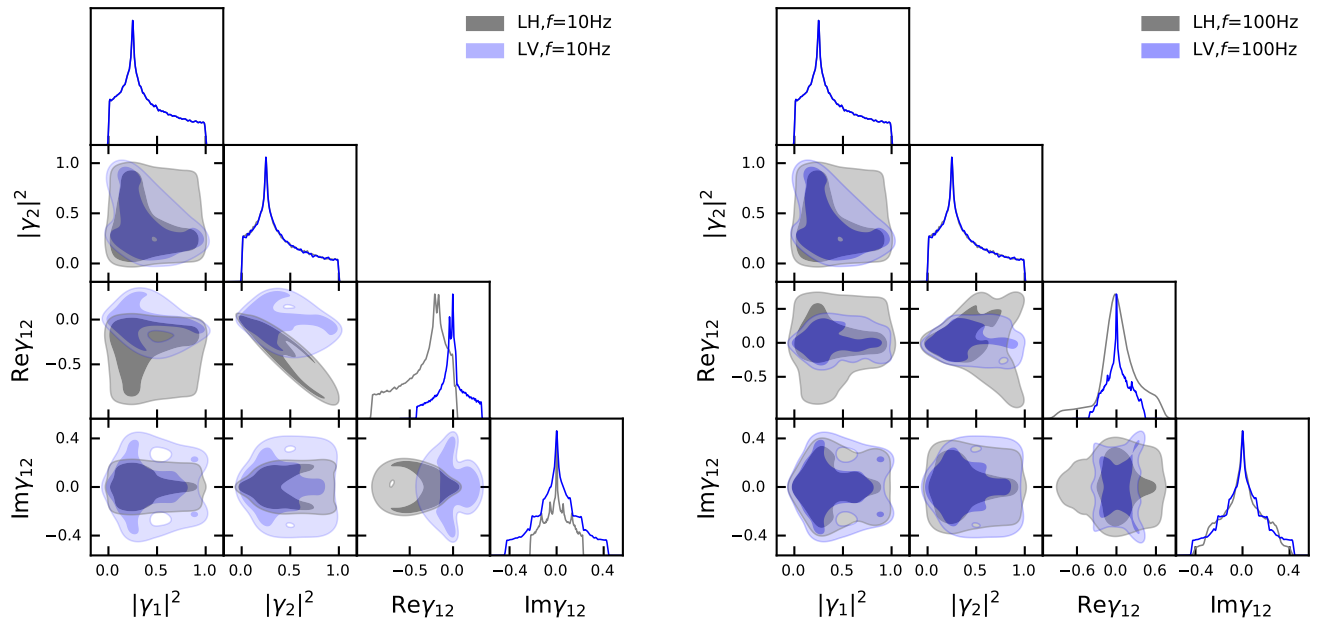


FIG. 2: Distributions of the quantities related to the GW detector projection vector  $\vec{y} = (|\gamma_1|^2, |\gamma_2|^2, \text{Re } \gamma_{12}, \text{Im } \gamma_{12})$  for isotropic source distribution. The gray color represents the detector pair LIGO-Livingston vs. LIGO-Hanford, while the blue color represents the detector pair LIGO-Livingston vs. Virgo. The left and right panels correspond to 10Hz and 100Hz, respectively.

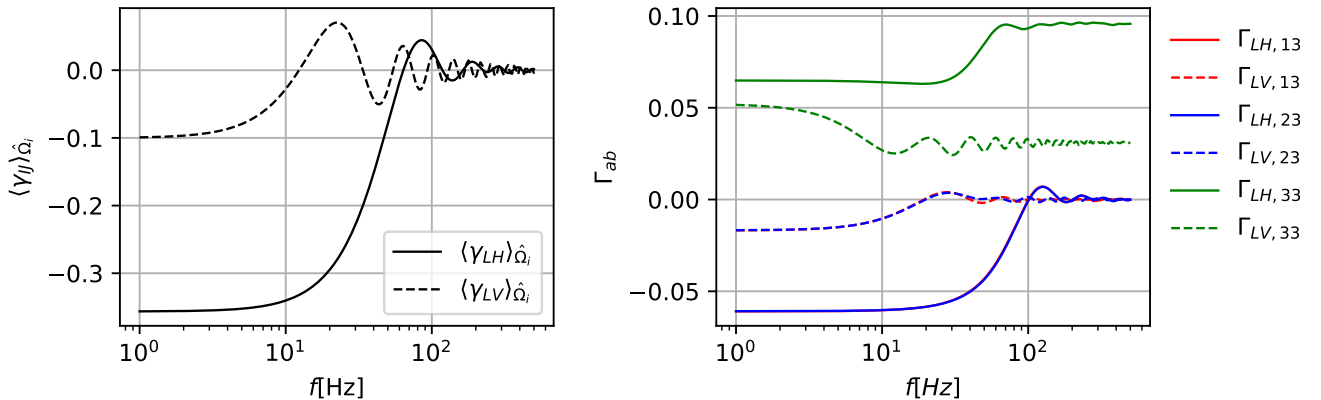


FIG. 3: Frequency dependence of the mean and the second-order covariance matrix elements of  $\vec{y}$  for an isotropic source distribution. Left panel: The sky-averaged overlap reduction function of  $\langle \gamma_{IJ}(f, \hat{\Omega}_i) \rangle_{\hat{\Omega}_i}$ , which is related to the standard overlap reduction function by  $\langle \gamma_{IJ}(f, \hat{\Omega}_i) \rangle_{\hat{\Omega}_i} = 2\tilde{\gamma}_{12}(f)/5$ . Right panel: The second-order covariance matrix elements  $\Gamma_{ab}$ , with different colors representing different components. Solid lines correspond to the LIGO-Livingston vs. LIGO-Hanford detector pair, while dashed lines represent the LIGO-Livingston vs. Virgo pair. Note that the lines corresponding to the (1,3) and (2,3) elements are overlapping.

which suggests that the fourth-order distribution property of the signals  $\tilde{s}_{I,i}$  are determined by the second-order covariance matrix  $\Gamma_{ab}$ .

Fig. 1 provides an intuitive illustration of how the antenna pattern function deforms the distribution of strain amplitude. Assuming the Hanford detector  $H_1$  as an example, we simulate a GWB with the original signal

strain amplitude drawn from a Gaussian distribution, and examine their projected distributions in the detector at 10Hz, assuming an isotropic source distribution for  $p_{\Omega}(\hat{\Omega}_i)$ . In the figure, we can observe that the original distribution  $\text{Re } h_+$  is deformed after the projection  $\hat{s}_{H_1} = \text{Re}(\gamma_{H_1} \tilde{h}_{H_1})$ , corresponding to the gray and green histograms, respectively. We also plot three theoretical probability density functions: the full integral expression

of Eq. (27), denoted as  $\mathcal{G}_I$ ; the leading-order expansion (the first term of Eq. (31)), which reduces to the Gaussian distribution  $\mathcal{G}$ ; and the corrected distribution  $\mathcal{G}_C$  (the first and second terms of Eq. (31)). The projected signal exhibits a clear deviation from Gaussianity, showing pronounced positive kurtosis, and inclusion of the second-order correction significantly improves agreement with the simulated distribution.

For stochastic backgrounds, cross-correlation depends on the combined response of two detectors, quantified by the overlap reduction function. This function incorporates the phase difference between spatially separated detectors, which varies with GW frequency. Consequently, the projection effect is inherently frequency dependent.

In Fig. 2, assuming an isotropic source distribution, we show the components of the GW detector projection vector,  $\vec{y} = (|\gamma_1|^2, |\gamma_2|^2, \text{Re } \gamma_{12}, \text{Im } \gamma_{12})$ , which directly characterize the projection effect on a stochastic background. The values are computed assuming a uniform source distribution for two detector pairs: LIGO–Livingston vs. LIGO–Hanford, and LIGO–Livingston vs. Virgo. The left and right panels correspond to 10 Hz and 100 Hz, respectively. All quantities exhibit distinctive, non-trivial structures, and the detector response distribution varies significantly with both the choice of detector pair and the frequency.

Fig. 3 illustrates the frequency dependence of the covariance matrix elements. For reference, the sky-averaged overlap reduction function,  $\langle \gamma_{IJ}(f, \hat{\Omega}_i) \rangle_{\hat{\Omega}_i}$ , is shown in the left panel. We recall that it is related to the usual sky-averaged overlap reduction function by  $\langle \gamma_{IJ}(f, \hat{\Omega}_i) \rangle_{\hat{\Omega}_i} = 2\bar{\gamma}_{12}(f)/5$ . The right panel displays the elements of the second-order covariance matrix  $\Gamma_{ab}$ . The (3,3) element, corresponding to the variance of  $\text{Re } \gamma_{12}$ , shows little variation with frequency and eventually stabilizes at a non-zero value. In contrast, (1,3) and (2,3) elements, corresponding to the covariances between  $|\gamma_1|^2$  or  $|\gamma_2|^2$  and  $\text{Re } \gamma_{12}$ , exhibit frequency-dependent behavior similar to that of the overlap reduction function. Although not shown in the figure, the fourth component,  $\text{Im}(\gamma_{12})$ , exhibits a similar trend.

### B. Effect of anisotropy

The choice of the form of  $p_\Omega$  is a prior assumption. In this section, we evaluate the impact of a non-isotropic  $p_\Omega$  on the observable vector  $\vec{y}$ . While a uniform distribution is a reasonable assumption for extragalactic BBH systems, future scenarios involving observation of white dwarf background with space detectors [51], or exotic models such as clustering of sub-solar mass primordial black hole binaries [52, 53] or cosmic strings [54] may necessitate consideration of the highly non-uniform spatial distribution of sources within the Milky Way. To quickly illustrate the effect of anisotropy, we introduce a simple

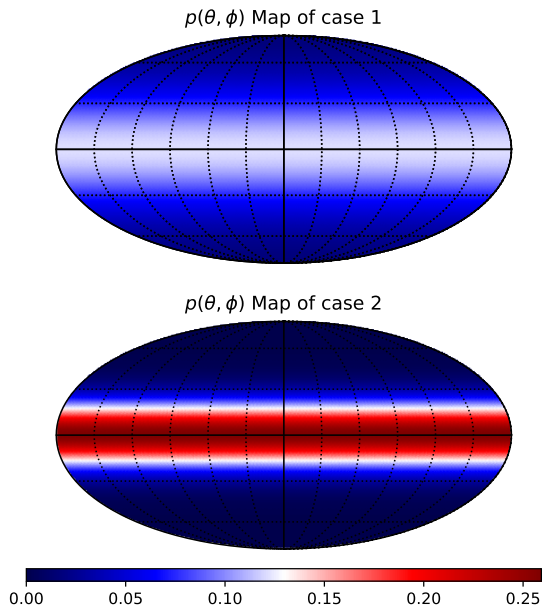


FIG. 4: A sky map illustrating the distribution of the toy-model anisotropic GWB. The top panel corresponds to the  $a_1$  model, characterized by a non-uniform distribution with  $\sigma_\Omega^2 = 0.06$ , while the bottom panel shows the  $a_2$  model with  $\sigma_\Omega^2 = 0.25$ .

toy model that mimics the structure of the galactic plane:

$$p_\Omega \sim \exp \left[ -\frac{\cos^2 \theta}{2\sigma_\Omega^2} \right], \quad (39)$$

where  $\theta$  represents the galactic latitude. Based on current observations, the luminous mass distribution of the Milky Way decreases significantly around  $\theta \sim 10^\circ$ . We consider two distributions with  $\sigma_\Omega^2 = 0.06$  and  $0.25$ , labeled as  $a_1$  and  $a_2$ , respectively, representing a more concentrated and a more diffuse distribution. These two distributions are shown in Fig. 4.

In Fig. 5, we present the distribution of  $\vec{y}$  for the LIGO–Livingston vs. LIGO–Hanford detector pair under two anisotropic source distributions. For comparison, we also plot results for an isotropic distribution. The figure indicates that anisotropy in the source distribution has only a minor impact on the distribution of  $\vec{y}$ . Noticeable deviations occur mainly in the tails of the distribution, particularly for the  $a_2$  model, which exhibits strong anisotropy. Fig. 6 compares the frequency dependence of the overlap reduction function and the second-order covariance matrix elements between the isotropic case and two anisotropic models. The  $a_2$  model exhibits up to a 30% variation in these quantities.

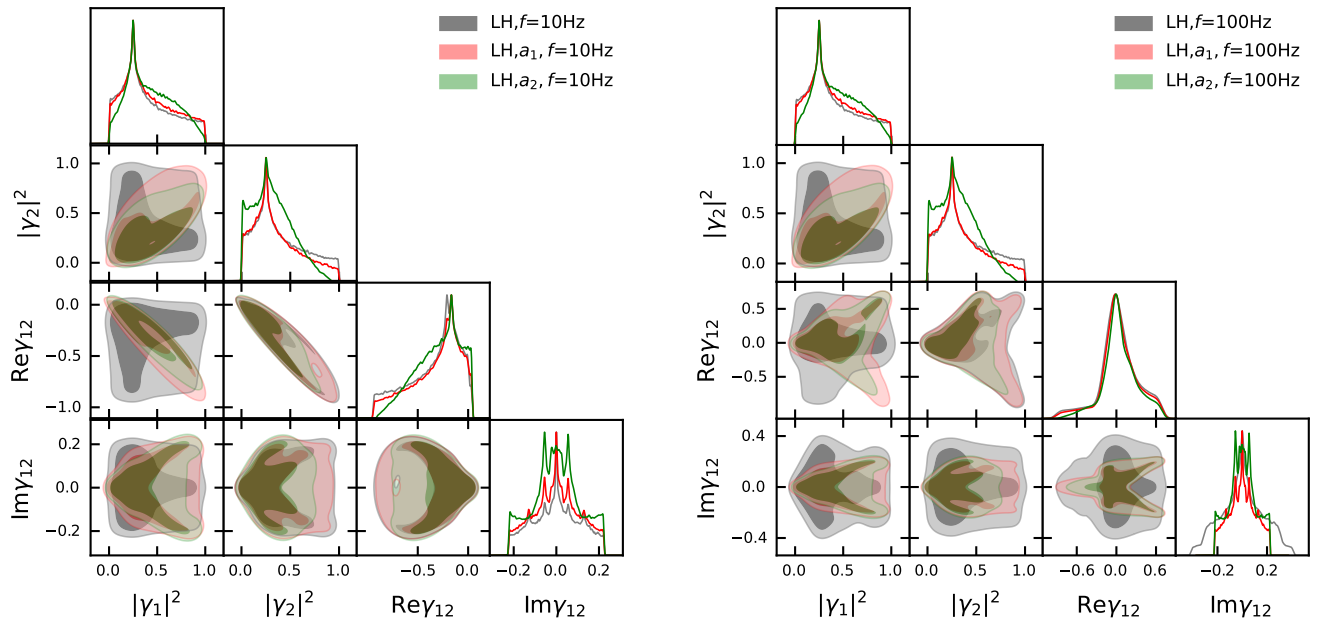


FIG. 5: Distributions of  $\vec{y} = (|\gamma_1|^2, |\gamma_2|^2, \text{Re } \gamma_{12}, \text{Im } \gamma_{12})$ , comparing the cases of isotropic and anisotropic source distributions. Grey indicates the isotropic distribution, red corresponds to the anisotropic distribution with  $\sigma_\Omega^2 = 0.25$ , and green corresponds to the anisotropic distribution with  $\sigma_\Omega^2 = 0.06$ . The detector pair assumed is LIGO-Livingston vs. LIGO-Hanford. The left and right panels show the results at 10Hz and 100Hz, respectively.

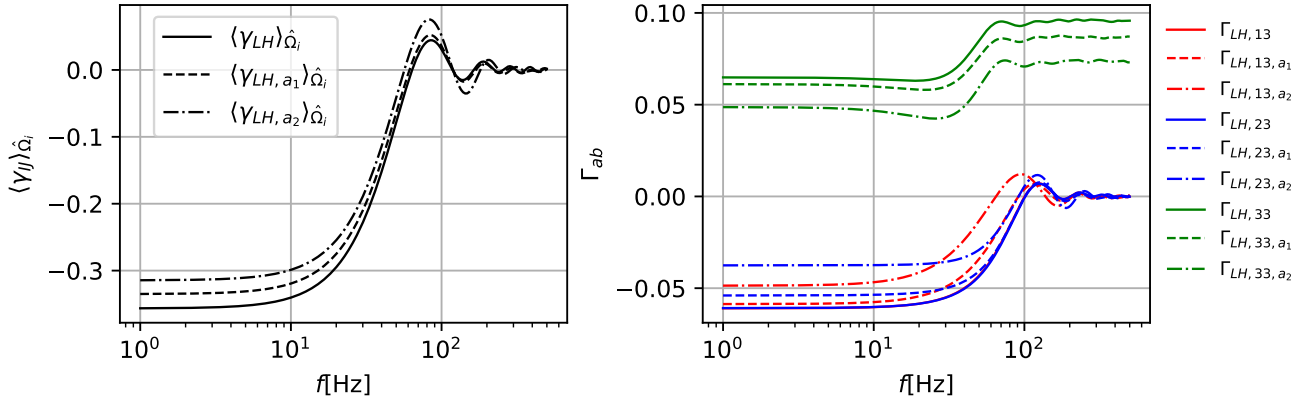


FIG. 6: Frequency dependence of the mean and the second-order covariance matrix elements of  $\vec{y}$ , comparing isotropic and anisotropic source distribution assumptions. Left panel: The sky-averaged overlap reduction function of  $\langle \gamma_{IJ}(f, \hat{\Omega}_i) \rangle_{\hat{\Omega}_i}$ . Right panel: The second-order covariance matrix elements, with different colors representing different components. Solid lines correspond to the uniform distribution, dashed lines to the anisotropic distribution with  $\sigma_\Omega^2 = 0.25$ , and dash-dotted lines to the anisotropic distribution with  $\sigma_\Omega^2 = 0.06$ .

#### IV. SIMULATED SIGNAL DETECTION AND PARAMETER ESTIMATION

Here, we simulate the detection of an intermittent GWB signal using the `pygwb` module [55] to demonstrate that neglecting the antenna pattern function can introduce biases in parameter estimation. First, we consider an isotropic source distribution, and then we investigate

whether anisotropy in the source distribution influences parameter estimation.

##### A. Isotropic source distribution

We consider the antenna pattern functions of LIGO-Livingston and LIGO-Hanford. The data segment length

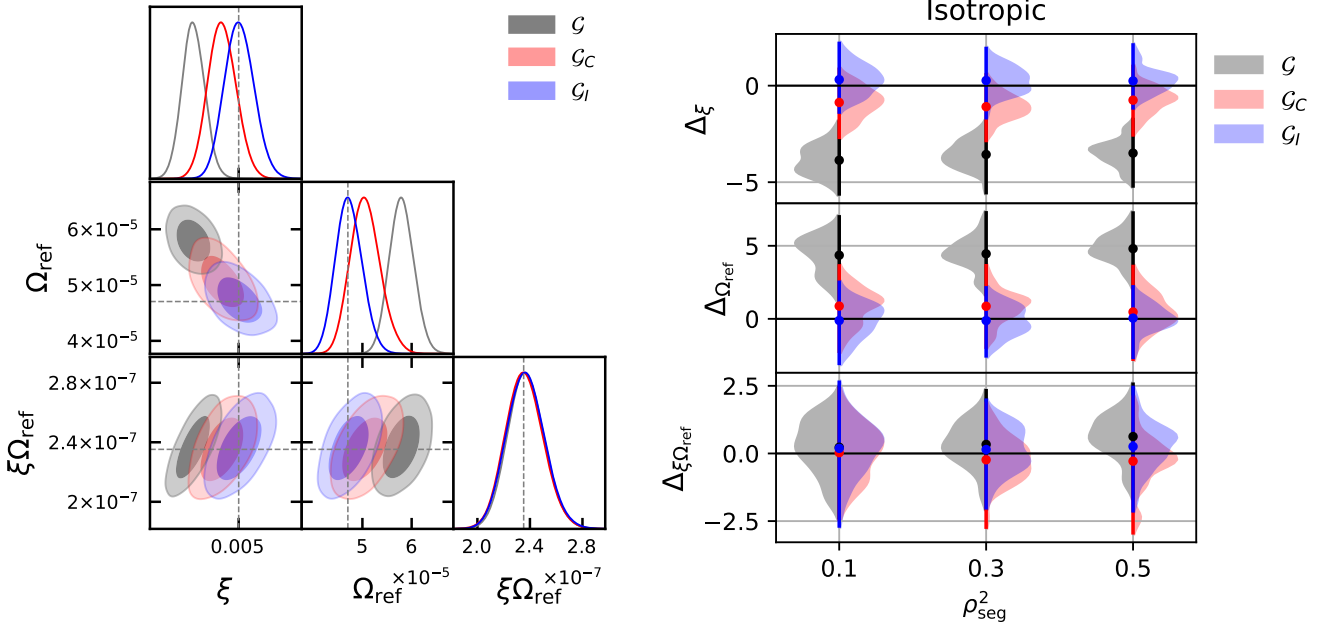


FIG. 7: Result of the isotropic case. Left panel: Posterior probability distribution of the parameters obtained from a single simulation with  $\rho_{\text{seg}}^2 = 0.1$ . Right panel: Comparison of the biases ( $\Delta_\xi$ ,  $\Delta_{\Omega_{\text{ref}}}$ ,  $\Delta_{\xi\Omega_{\text{ref}}}$ ) for three likelihood models: the uncorrected Gaussian model ( $\mathcal{G}$ , black), the model with numerically integrated  $p_\Omega$  ( $\mathcal{G}_I$ , blue), and the model with covariance matrix  $\Gamma_{ab}$  corrections ( $\mathcal{G}_C$ , red). The histograms are shown for different SNRs  $\rho_{\text{seg}}^2 \sim (0.1, 0.3, 0.5)$ , each based on results from 50 simulations.

is set to  $T_{\text{seg}} = 4\text{s}$ , and the total number of data segments is 100000, corresponding to an observation time of approximately four days. We assume the duty cycle to be  $\xi = 0.005$ , so the number of segments containing GW signals is 500. We assume that the original distribution of GW signals to be Gaussian and the signal power spectrum is given by  $P_H \propto f^{-7/3}$ , then the GWB density parameter is given by

$$\Omega_{\text{gw}} = \xi\Omega_{\text{ref}} \left( \frac{f}{f_{\text{ref}}} \right)^{2/3}, \quad (40)$$

where the reference frequency is chosen as  $f_{\text{ref}} = 25\text{Hz}$ . These GWs are isotropically distributed, specifically,

$$\alpha \sim U(0, 2\pi), \cos\left(\frac{\pi}{2} - \delta\right) \sim U(-1, 1), \psi \sim U(0, \pi).$$

We define the averaged correlated SNR for a single segment  $\rho_{\text{seg}}$  as

$$\rho_{\text{seg}} := \sqrt{2T_{\text{seg}} \sum_{I,J} \int_{f_0}^{f_{\text{max}}} \frac{\gamma_{IJ}^2(f) P_H^2(f)}{P_{n_I}(f) P_{n_J}(f)} \, df}, \quad (41)$$

where  $P_H^2(f)$  is the averaged (squared) spectrum of the GW signal, obtained by averaging the GW signal spectrum over all segments, including both signal-containing and noise-only segments. Here, we choose  $f_0 = 10\text{Hz}$ , and assume identical white noise for both detectors. We

set  $\Omega_{\text{ref}} \approx 4.7 \times 10^{-5}$  and the noise level is set to produce  $\rho_{\text{seg}}^2 \sim (0.1, 0.3, 0.5)$ . Under this configuration, most of the GW signal intensity lies below the noise level. To reduce computation time, we selected only 5 frequency bins between 10Hz and 100Hz.

We consider three models for comparison: the original Gaussian likelihood model (labeled  $\mathcal{G}$ ), the likelihood model with a full integral over  $\hat{\Omega}$ , as given in Eq. (28) (labeled  $\mathcal{G}_I$ ), and the likelihood model expanded to include the second-order covariance matrix, as given in Eq. (31) (labeled  $\mathcal{G}_C$ ). Since the  $\mathcal{G}_I$  model involves integration, sampling process is more computationally demanding. Therefore, for this comparison, we exclude the estimation of the noise parameters for the two detectors, assuming their noise levels are known, and focus solely on parameter estimation of the two parameters: the duty cycle  $\xi$  and the signal amplitude  $\Omega_{\text{ref}} \propto \sigma_H^2$ . We assume uniform prior for  $\xi$  and log-uniform prior for  $\Omega_{\text{ref}}$ .

To assess the impact of stochastic variations in the simulations, we perform 50 repeated simulations. For each posterior distribution obtained from a single run, we compute the biases for each parameter ( $\Delta_\xi$ ,  $\Delta_{\Omega_{\text{ref}}}$ ) as well as the bias of the total GWB density  $\Delta_{\xi\Omega_{\text{ref}}}$ . Specifically, the bias  $\Delta_X$  of parameter  $X$  is defined as

$$\Delta_X := \frac{\langle X \rangle_{\text{post}} - X_{\text{inj}}}{\sigma_{X,\text{post}}}, \quad (42)$$

where  $\langle X \rangle_{\text{post}}$  is the posterior mean of  $X$ ,  $X_{\text{inj}}$  is the in-

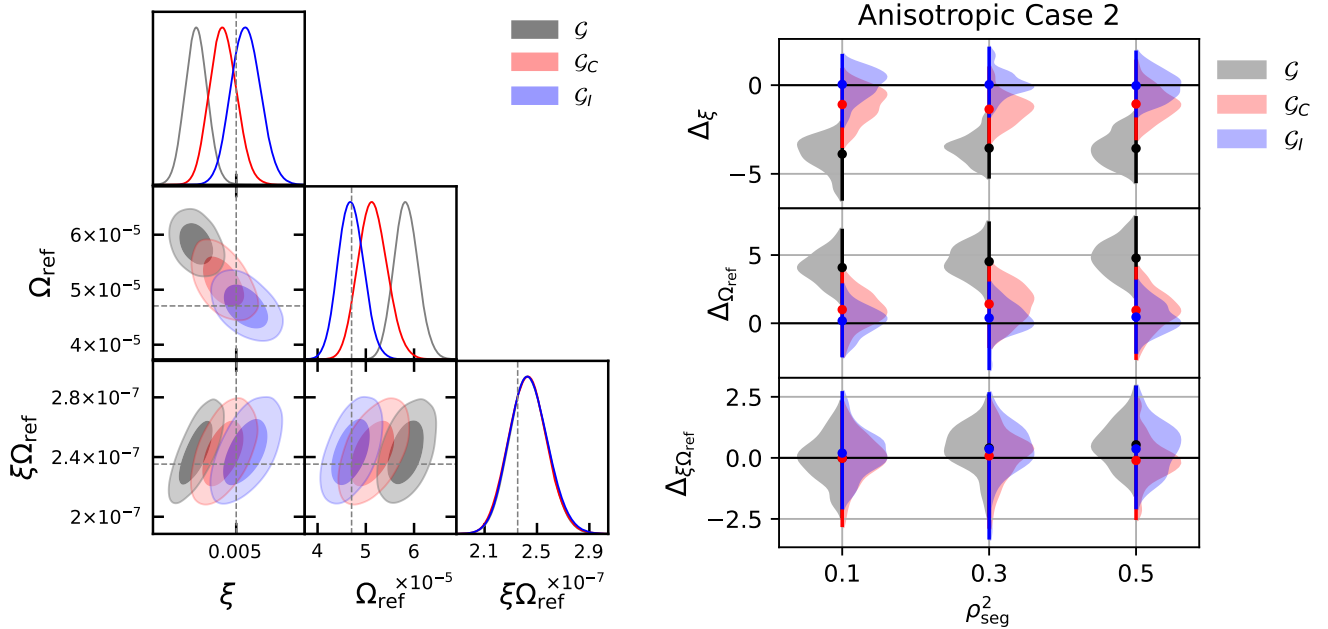


FIG. 8: Same as Fig. 7, except the data are generated under an anisotropic background assumption, while the analysis assumes an isotropic background.

jected parameter value, and  $\sigma_{X,\text{post}}^2$  is the variance of the marginalized posterior distribution of  $X$ . This quantity measures how many standard deviations ( $\sigma$ ) the inferred parameter value deviates from the true value, thereby characterizing the intrinsic capability of each model to recover the true parameters.

In Fig. 7, the left panel shows representative posterior distributions from a single selected simulation, while the right panel presents the bias distributions for each parameter  $(\Delta\xi, \Delta\Omega_{\text{ref}}, \Delta\xi\Omega_{\text{ref}})$  obtained from 50 simulations for different SNRs  $\rho_{\text{seg}}^2 \sim (0.1, 0.3, 0.5)$ . Results from multiple simulations on the right panel clearly indicate that the uncorrected Gaussian model  $\mathcal{G}$  introduces systematic biases regardless of SNR: specifically,  $\xi$  tends to be underestimated, while  $\Omega_{\text{ref}}$  is overestimated. The model using the full integral form,  $\mathcal{G}_I$ , effectively corrects these biases. We also find that the model incorporating the second-order covariance matrix correction,  $\mathcal{G}_C$ , produces results that are closer to those of the full integral model.

Another notable observation is that the overall posterior variance of the total GWB energy density,  $\Omega_{\text{gw}} \propto \xi\Omega_{\text{ref}}$ , remains essentially unbiased across all models. This is also seen in the left panel of Fig. 7, where the degeneracy between  $\xi$  and  $\Omega_{\text{ref}}$  appears to align along a direction that preserves the same  $\Omega_{\text{gw}}$  amplitude, specifically satisfying the relation  $\xi\Omega_{\text{ref}} = \text{const.}$

## B. Anisotropic source distribution

A natural question that arises is whether anisotropy in the GWB introduces additional bias in parameter estimation. To investigate this, we perform simulations using mock data generated under an anisotropic GWB assumption, while analyzing the data under the simplifying assumption of isotropy.

First, we create the data assuming the anisotropic distribution equivalent to the  $a_2$  model described in section III B,

$$\alpha \sim U(0, 2\pi), \cos\left(\frac{\pi}{2} - \delta\right) \sim \mathbf{G}[\sigma_\Omega^2]_{(-1,1)}, \psi \sim U(0, \pi),$$

where  $\mathbf{G}[\sigma_\Omega^2]_{(-1,1)}$  denotes the Gaussian distribution truncated within  $(-1, 1)$ , and  $\sigma_\Omega^2 = 0.06$ .

As in the previous subsection, we perform detection simulations for three different SNR cases,  $\rho_{\text{seg}}^2 \in 0.1, 0.3, 0.5$ , repeating each scenario 50 times. The resulting bias in the posterior probability distribution is shown in Fig. 8. This result shows almost no difference compared to the isotropic case shown in Fig. 7, indicating that even a strong level of anisotropy has no significant impact on parameter estimation. Therefore, in terms of parameter estimation accuracy, assuming an isotropic prior  $p_\Omega = 1/(4\pi)$  is sufficient.

However, we find that differences between isotropic and anisotropic assumptions appear in the Bayes factors. In Fig. 9, we compare the Bayes factors  $\Delta \ln Z$  for the  $\mathcal{G}_I$  and  $\mathcal{G}_C$  models relative to the  $\mathcal{G}$  model, based on distributions obtained from 50 simulations each. The

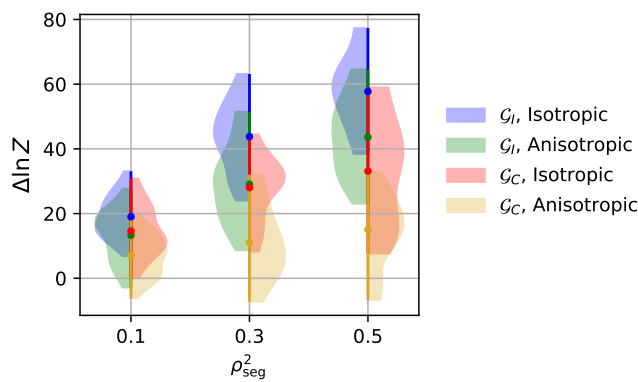


FIG. 9: Histograms of the Bayes factor ratios,  $\ln Z_{G_I}/Z_G$  and  $\ln Z_{G_C}/Z_G$ , are shown for isotropic and anisotropic cases for different SNRs.

Bayes factor of a model  $X$  is given by marginalizing the posterior probability distribution  $p_{\text{post}}(\boldsymbol{\theta})$  of the model parameters  $\boldsymbol{\theta}$ ,

$$Z_X = \int p_{\text{post}}(\boldsymbol{\theta})\pi(\boldsymbol{\theta})d\boldsymbol{\theta}, \quad (43)$$

where  $\pi(\boldsymbol{\theta})$  denotes the prior. The ratio  $\ln(Z_1/Z_2)$  quantifies the relative detection capability of two models; a higher Bayes factor indicates a more reliable model. From Fig. 9, we observe that in the isotropic case, both  $\mathcal{G}_I$  and  $\mathcal{G}_C$  exhibit higher Bayes factors compared to  $\mathcal{G}$ . Under anisotropic conditions, however, these ratios are reduced. This suggests that when sources are anisotropically distributed, using isotropic priors does not introduce bias in parameter estimates; however, it reduces the detection performance of the  $\mathcal{G}_I$  and  $\mathcal{G}_C$  models compared to  $\mathcal{G}$ .

## V. SUMMARY

The astrophysical GWB exhibits a highly non-Gaussian nature in the frequency band of ground-based detectors, posing unique challenges for analysis. In this work, we highlighted a critical aspect that must be considered when searching for such a non-Gaussian stochastic background: the detector antenna patterns, which enter the analysis through the overlap reduction function in the cross-correlation method.

We pointed out that the non-spherical nature of the antenna pattern functions of detectors modifies the statistical properties of the signal distribution. This effect is frequency-dependent when the two detectors are spatially separated, due to the phase difference between them. We showed that this modification generally introduces positive kurtosis in the signal distribution.

When constructing the likelihood function, this projection effect must be incorporated. However, incorporating

it requires an additional integration over the source direction, which significantly increases computational cost for parameter estimation because the likelihood must be evaluated at every sample point. To overcome this, we introduced a method that treats the effect as a higher-order moment expansion by utilizing the covariance matrix of the detector response function.

To compare parameter estimation performance, we simulated the detection and parameter estimation by generating mock data containing Gaussian burst signals. Three likelihood models were tested: the conventional Gaussian model, which averages the antenna pattern effect over the sky; the full integral formulation; and the corrected model with the second-order covariance matrix. The results show that the Gaussian model consistently underestimates the duty cycle and overestimates the variance of the GW amplitude, whereas the full integral formulation exhibits no deviation. We also demonstrated that the second-order correction effectively mitigates the bias in parameter estimation.

In addition, we investigated the effect of anisotropic source distributions. The detector response function and its covariance matrix show slight differences when anisotropy is present. Finally, we examined whether assuming an isotropic source distribution in the analysis introduces bias in the estimated parameters when the true background is anisotropic. Through detailed simulations, we found no such bias in parameter estimation. However, we observed that the Bayes factors decrease when the source distribution is anisotropic, even though no parameter bias occurs.

This study focused on the impact of detector response in intermittent searches, using simulations based on Gaussian-distributed, burst-like data. In contrast, the most probable astrophysical background signal originates from BBH mergers, which pose additional challenges due to their complex, non-Gaussian characteristics arising from source population characteristics and waveform structures. In future work, we will address more realistic scenarios by modeling CBC sources and systematically tackling these challenges to ensure that we are prepared to analyze the forthcoming observational data.

## Acknowledgments

We thank David Alonso, Neil Cornish, Federico De Lillo, Jessica Lawrence, Guo Chin Liu, Nick Van Remortel, Arianna Renzini, Joseph Romano, and Takahiro Yamamoto for very helpful discussion. XL and SK are supported by the I+D grant PID2023-149018NB-C42 and the Grant IFT Centro de Excelencia Severo Ochoa No CEX2020-001007-S, funded by MCIN/AEI/10.13039/501100011033, the Leonardo Grant for Scientific Research and Cultural Creation 2024 from the BBVA Foundation, and Japan Society for JSPS KAKENHI Grant no. JP23H00110 and JP24K00624.

---

[1] J. Aasi et al. (LIGO Scientific), *Class. Quant. Grav.* **32**, 074001 (2015), 1411.4547.

[2] F. Acernese et al. (VIRGO), *Class. Quant. Grav.* **32**, 024001 (2015), 1408.3978.

[3] T. Akutsu et al. (KAGRA), *PTEP* **2021**, 05A101 (2021), 2005.05574.

[4] R. Abbott et al. (LIGO Scientific, Virgo), *Phys. Rev. X* **11**, 021053 (2021), 2010.14527.

[5] R. Abbott et al. (KAGRA, VIRGO, LIGO Scientific), *Phys. Rev. X* **13**, 041039 (2023), 2111.03606.

[6] A. G. Abac et al. (LIGO Scientific, VIRGO, KAGRA) (2025), 2508.18083.

[7] M. Punturo et al., *Class. Quant. Grav.* **27**, 194002 (2010).

[8] M. Evans et al. (2021), 2109.09882.

[9] M. Colpi et al. (LISA) (2024), 2402.07571.

[10] J. Luo et al. (TianQin), *Class. Quant. Grav.* **33**, 035010 (2016), 1512.02076.

[11] W.-H. Ruan, Z.-K. Guo, R.-G. Cai, and Y.-Z. Zhang, *Int. J. Mod. Phys. A* **35**, 2050075 (2020), 1807.09495.

[12] S. Kawamura et al., *PTEP* **2021**, 05A105 (2021), 2006.13545.

[13] J. D. Romano and N. J. Cornish, *Living Rev. Rel.* **20**, 2 (2017), 1608.06889.

[14] N. van Remortel, K. Janssens, and K. Turbang, *Prog. Part. Nucl. Phys.* **128**, 104003 (2023), 2210.00761.

[15] A. G. Abac et al. (LIGO Scientific, VIRGO, KAGRA) (2025), 2508.20721.

[16] K. Belczynski, V. Kalogera, and T. Bulik, *Astrophys. J.* **572**, 407 (2001), astro-ph/0111452.

[17] H. A. Bethe and G. E. Brown, *Astrophys. J.* **506**, 780 (1998), astro-ph/9802084.

[18] B. Allen and J. D. Romano, *Phys. Rev. D* **59**, 102001 (1999), gr-qc/9710117.

[19] N. J. Cornish and J. D. Romano, *Phys. Rev. D* **92**, 042001 (2015), 1505.08084.

[20] B. P. Abbott et al. (LIGO Scientific, Virgo), *Phys. Rev. Lett.* **116**, 131102 (2016), 1602.03847.

[21] B. P. Abbott et al. (LIGO Scientific, Virgo), *Phys. Rev. Lett.* **120**, 091101 (2018), 1710.05837.

[22] D. Coward and T. Regimbau, *New Astron. Rev.* **50**, 461 (2006), astro-ph/0607043.

[23] M. Braglia, J. Garcia-Bellido, and S. Kuroyanagi, *Mon. Not. Roy. Astron. Soc.* **519**, 6008 (2023), 2201.13414.

[24] S. Drasco and E. E. Flanagan, *Phys. Rev. D* **67**, 082003 (2003), gr-qc/0210032.

[25] E. Thrane, *Phys. Rev. D* **87**, 043009 (2013), 1301.0263.

[26] J. Lawrence, K. Turbang, A. Matas, A. I. Renzini, N. van Remortel, and J. D. Romano, *Phys. Rev. D* **107**, 103026 (2023), 2301.07675.

[27] R. Buscicchio, A. Ain, M. Ballelli, G. Cella, and B. Patricelli, *Phys. Rev. D* **107**, 063027 (2023), 2209.01400.

[28] M. Ballelli, R. Buscicchio, B. Patricelli, A. Ain, and G. Cella, *Phys. Rev. D* **107**, 124044 (2023), 2212.10038.

[29] N. Seto, *Astrophys. J. Lett.* **683**, L95 (2008), 0807.1151.

[30] N. Seto, *Phys. Rev. D* **80**, 043003 (2009), 0908.0228.

[31] L. Martellini and T. Regimbau, *Phys. Rev. D* **89**, 124009 (2014), 1405.5775.

[32] L. Martellini and T. Regimbau, *Phys. Rev. D* **92**, 104025 (2015), [Erratum: *Phys. Rev. D* **97**, 049903 (2018)], 1509.04802.

[33] A. Sasli, N. Karnesis, and N. Stergioulas, *Phys. Rev. D* **108**, 103005 (2023), 2305.04709.

[34] R. Smith and E. Thrane, *Phys. Rev. X* **8**, 021019 (2018), 1712.00688.

[35] R. J. E. Smith, C. Talbot, F. Hernandez Vivanco, and E. Thrane, *Mon. Not. Roy. Astron. Soc.* **496**, 3281 (2020), 2004.09700.

[36] S. Biscoveanu, C. Talbot, E. Thrane, and R. Smith, *Phys. Rev. Lett.* **125**, 241101 (2020), 2009.04418.

[37] X.-X. Kou, M. Saleem, V. Mandic, C. Talbot, and E. Thrane, *Phys. Rev. D* **112**, 084064 (2025), 2506.14179.

[38] R. Dey, L. F. Longo Micchi, S. Mukherjee, and N. Afshordi, *Phys. Rev. D* **109**, 023029 (2024), 2305.03090.

[39] M. R. Sah and S. Mukherjee (2023), 2307.06405.

[40] M. R. Sah and S. Mukherjee (2025), 2511.03262.

[41] A. Utina, F. Marangio, F. Morawski, A. Iess, T. Regimbau, G. Fiameni, and E. Cuoco, in *International Conference on Content-Based Multimedia Indexing* (2021).

[42] T. S. Yamamoto, S. Kuroyanagi, and G.-C. Liu, *Phys. Rev. D* **107**, 044032 (2023), 2208.13156.

[43] W. G. Lamb and S. R. Taylor, *Astrophys. J. Lett.* **971**, L10 (2024), 2407.06270.

[44] G. Franciolini, M. Pieroni, A. Ricciardone, and J. D. Romano (2025), 2505.24695.

[45] P. A. Rosado, *Phys. Rev. D* **84**, 084004 (2011), 1106.5795.

[46] P. Jaranowski, A. Krolak, and B. F. Schutz, *Phys. Rev. D* **58**, 063001 (1998), gr-qc/9804014.

[47] E. Thrane, S. Ballmer, J. D. Romano, S. Mitra, D. Talukder, S. Bose, and V. Mandic, *Phys. Rev. D* **80**, 122002 (2009), 0910.0858.

[48] B. Allen and A. C. Ottewill, *Phys. Rev. D* **56**, 545 (1997), gr-qc/9607068.

[49] A. Matas and J. D. Romano, *Phys. Rev. D* **103**, 062003 (2021), 2012.00907.

[50] F. W., *An introduction to probability theory and its applications Volume 1* (Wiley, 1968), 3rd ed., URL [libgen.li/file.php?md5=b5ca41bdbca3ccb153e7e271521d7bec](http://libgen.li/file.php?md5=b5ca41bdbca3ccb153e7e271521d7bec).

[51] C. L. Fryer, K. Belczynski, G. Wiktorowicz, M. Dominik, V. Kalogera, and D. E. Holz, *Astrophys. J.* **749**, 91 (2012), 1110.1726.

[52] F. van Die, I. Rapoport, Y. B. Ginat, and V. Desjacques, *JCAP* **05**, 036 (2025), 2410.04522.

[53] S. Afroz and S. Mukherjee (2025), 2507.22126.

[54] T. Regimbau, S. Giampaolis, X. Siemens, and V. Mandic, *Phys. Rev. D* **85**, 066001 (2012), 1111.6638.

[55] A. I. Renzini et al., *Astrophys. J.* **952**, 25 (2023), 2303.15696.